Contrasting sensitivity of weathering proxies to Quaternary climate and sea-level fluctuations in the southern South China Sea

Yi Zhong [1, 2 3, 4], David J. Wilson [5], Jiabo Liu [1, 3, 4], Shiming Wan [6], Rui Bao [7], Jianxing Liu [8], Yanan Zhang [1], Xuesong Wang [2], Yuanhao Liu [1], Xiaoyu Liu [1], Ying Zhao [1], Shiying Li [9], Qingsong Liu [1, 3, 4*]

[1] Centre for Marine Magnetism (CM^2), Department of Ocean Science and Engineering, Southern University of Science and Technology, Shenzhen 518055, PR China

[2] Key Laboratory of Ocean and Marginal Sea Geology, South China Sea Institute of Oceanology, Chinese Academy of Sciences, Guangzhou 510301, China

[3] Laboratory for Marine Geology, Qingdao National Oceanography Laboratory for Marine Science and Technology, Qingdao 266061, China

[4] Southern Marine Science and Engineering Guangdong Laboratory (Guangzhou), Guangzhou, China

[5] Institute of Earth and Planetary Sciences, University College London and Birkbeck, University of London, London, UK

[6] Key laboratory of Marine Geology and Environment, Institute of Oceanology, Chinese Academy of Sciences, Qingdao 266071, China

[7] Key Laboratory of Marine Chemistry Theory and Technology, Ministry of Education/Institute for Advanced Ocean Studies, Ocean University of China, Qingdao, China

[8] Key Laboratory of Marine Sedimentology and Environmental Geology, First Institute of Oceanography, Ministry of Natural Resources (MNR), Qingdao, China

[9] Guangdong Marine Geological Survey, Guangzhou 510080, China

[*]Corresponding author: qsliu@sustech.edu.cn

Key Points:

In the southern South China Sea, clay mineralogy responds rapidly to climate-driven changes in inputs on orbital timescales.

Magnetic content within the coarser fraction is more strongly influenced by sea-level change, through bedload and resuspension transport.

This depositional framework may serve as a guideline for evaluating sea-level change on continental shelves over orbital timescales.

Abstract

Tropical marginal seas host important sedimentary archives that may be exploited to reveal past changes in continental erosion, chemical weathering, and ocean dynamics. However, these records can be challenging to interpret due to the complex interactions between climate and particulate transport across ocean margins. For the southern South China Sea over the last 90 kyr, we observe a contrasting temporal relationship between the deposition of clay minerals and magnetic minerals, which were associated with two different hydrodynamic modes. Fine-grained clay minerals can be carried in suspension by ocean currents, leading to a rapid response to regional climate-driven inputs. In contrast, changes in magnetic mineralogy were associated with bedload transport and resuspension, leading to a control by glacial-interglacial sea-level variability. Overall, this study indicates that the transfer pathways and mechanisms imparted by varying hydrodynamic conditions exert a substantial influence on the distribution of terrigenous material in continental shelf and margin sediments.

Plain Language Summary

Sediments that accumulate in the ocean along continental margins contain the minerals that were eroded and transported by rivers on the nearby land masses. Past changes in the composition of such sediments can be used to reconstruct the history of physical erosion and chemical weathering on the continents, but can also be affected by ocean dynamics over orbital and millennial timescales. Here, clay mineralogy, sediment grain size, and rock magnetic signatures were measured in a core from the continental slope of the southern South China Sea, spanning the last 90 thousand years. Differences between the clay mineral and magnetic records, which are linked to finer and coarser sediment fractions respectively, indicate that specific mechanisms and timescales influenced sediment transport to the core site. This depositional framework must be considered when interpreting the timing of changes in weathering and erosion proxies hosted in sediment records from marginal seas. Specifically, fine-grained clay minerals may reveal a rapid response to continental weathering changes, whereas the magnetic records are influenced by the transport of coarser-grained minerals under the influence of sea-level change. In addition, this framework could potentially serve as an indicator of past sea-level change on continental shelves.

Introduction

While continental margins and marginal seas account for only ~10-20% of the global ocean area, many are located in highly dynamic regions in which elevated physical erosion, chemical weathering, and organic carbon burial play a major role in the global carbon cycle (Wan et al., 2009). Moreover, continental margins are characterised by rapid sediment accumulation, such that high-

resolution records of past weathering and erosion can potentially be obtained by deciphering the geochemical and mineralogical signatures within these sedimentary successions. Hence, these regions are of great strategic value for research into continent-ocean interactions and paleoclimate variations over millennial and orbital timescales (Wan et al., 2017; Xu et al., 2021). However, a detailed understanding of the controls on sediment transport, deposition, and burial in these complex environments is a prerequisite for interpreting these sedimentary records and recognizing their implications for the global carbon cycle (Wan et al., 2012; Xu et al., 2018).

Due to their physico-chemical properties, such as mineral surface area and cation exchange capacity, terrestrial minerals play a crucial role in governing the amount and type of organic matter ultimately preserved in ocean sediments (Blattmann et al., 2019). Moreover, particle resuspension and lateral advection of sediment within nepheloid layers (Oliveira et al., 2002; Quaresma et al., 2007) may generate disparities in the spatial distribution of terrestrial minerals with differing grain-size associations due to hydrodynamic sorting (Ohkouchi et al., 2002; Thomsen & Gust, 2000). Therefore, in the Chinese marginal seas, terrigenous organic carbon transport, distribution, and preservation are largely determined by hydrodynamic sorting processes (Bao et al., 2018). However, the impact of these processes on interpretations of paleoclimate and weathering signals documented in sediment records from the marginal seas has received less attention and is less well understood.

Climate fluctuations during Quaternary glacial-interglacial cycles have significantly influenced the flux and composition of terrigenous sediment supplied to continental shelves, slopes, and deep-sea basins, modulated both by changes in precipitation and runoff and by sea-level fluctuations (Griffiths et al., 2009; Steinke et al., 2008). For example, studies based on clay mineralogy and sediment geochemistry in the tropical marginal seas (e.g. Arabian Sea, Bay of Bengal, and South China Sea) have revealed increases in terrigenous detrital input, organic carbon burial, and marine productivity during glacial periods, which were linked to the exposure of continental shelves (Xu et al., 2020; 2021). Because of the association of different terrigenous minerals with different sedimentary grain-size fractions (Bao et al., 2019), definitive evidence to test such a sea-level hypothesis could be obtained through targeted mineralogical investigations which would enable attribution to hydrodynamic sorting.

The southern South China Sea (SCS), together with the wide Sunda Shelf, is suitable for exploring the effects of sea-level change on terrigenous sediment input (Text S1) because this region receives large fluvial sediment fluxes and has been dramatically influenced by sea-level rise during the deglacial and early Holocene periods (Figure 1) (Hanebuth & Stattegger, 2004; Hanebuth et al., 2002; Milliman et al., 1999). Here, we compare grain size, clay mineralogy, and magnetic mineralogy records from the southern SCS over the last 90 kyr in order to assess the prevalence and nature of hydrodynamic mineral-sorting influences on the sedimentary archive. Our findings underscore an important link between

regional hydrodynamics and the depositional patterns of weathering and erosion indicators in the marginal seas.

1.

Materials and methods

(a)

Materials

The studied sediment core HYIV2015-B9 (hereafter referred to as B9; 10.2484°N, 112.7325°E; 2603 m water depth) was retrieved from the northern slope of Nasha Terrace in the southern SCS (Figure 1 and S1) during cruise HYIV20150816 of *R/V Haiyang IV* in 2015. The core is 4.25 m long and is dominated by homogenous dark grey clay without visible bioturbation. The age model for core B9 was constrained by 9 AMS ^{14}C dates of planktonic foraminifera in the upper part (< 170 cm) (Li et al., 2018a) (Figure S2 and S3). The chronology for the deeper part was established in this study by correlating the benthic foraminiferal *C. wuellerstorfi* ^{18}O record to the LR04 benthic foraminiferal ^{18}O stack (Lisiecki & Raymo, 2005), supported by variations in the elemental Ca/Al ratios in core B9 where the benthic ^{18}O record was less well resolved (Figure S2 and S3; Text S2 in the supporting information). Overall, the core provides a continous sedimentary record extending from the Holocene back to early marine isotope stage (MIS) 5 (~90 ka BP), with sedimentation rates varying from 1.8 to 7.3 cm/kyr (Text S2 in the supporting information).

Methods

For foraminiferal oxygen and carbon isotope measurements, epifaunal benthic foraminifera *Cibicidoides wuellerstorfi* were picked from the >150 m size fraction at 2 to 4 cm intervals, and ^{18}O and ^{13}C values were measured on a Thermo Scientific MAT 253 mass spectrometer, with calibration to the Pee Dee Belemnite (PDB) standard. For the elemental analysis, approximately 2-g freeze-dried sediments were taken at 1 to 4 cm intervals and crushed into powder. Following digestion in a mixture of HF and HNO_3, major element abundances were determined using ICP-OES (IRIS Intrepid II XSP) following the methodology of Qi et al. (2000). The accuracy of this method, determined by analysing standard reference materials (Chinese marine sediments GBW 07315 and GBW 07316, and U.S. Geological Survey basalt BHVO-2), is better than 3%.

A total of 225 samples were taken at 2-cm intervals to perform grain size, clay mineralogical composition, and rock magnetic analysis. The grain-size distribution of the detrital fraction was measured using a Malvern Mastersizer 3000G laser diffraction particle analyzer with a measurement range of 0.01-2000 m and 0.25 Φ interval resolution. Clay mineral studies were conducted on the < 2 m fraction of samples, following the removal of organic matter and carbonate

by treating with hydrogen peroxide (15%) and acetic acid (25%). Clay mineral analysis was conducted by X-ray diffraction (XRD) using a D8 ADVANCE diffractometer with CuK (alpha) radiation (40 kV, 40 mA).

A series of environmental magnetism parameters were measured and calculated for the samples of core B9, including magnetic susceptibility ( ), anhysteretic remanent magnetization susceptibility ($_{\mathrm{ARM}}$), saturated isothermal remanent magnetization (SIRM), $_{\mathrm{ARM}}$/SIRM, hard (high-coercivity) saturated isothermal remanent magnetization ($\mathrm{HIRM}_{300\mathrm{mT}}$), S-ratio, and L-ratio. The $\mathrm{HIRM}_{300\mathrm{mT}}$ parameter, which is defined as $\mathrm{HIRM}_{300\mathrm{mT}} = (\mathrm{SIRM}_{1.0\mathrm{T}} + \mathrm{IRM}_{\text{-}300\mathrm{mT}})/2$, is used to distinguish the contributions of hematite and goethite from those of magnetite (Liu et al., 2007). The S-ratio ($\mathrm{S}_{\text{-}300\mathrm{mT}}$), which is defined as the ratio of $\mathrm{IRM}_{\text{-}300\mathrm{mT}}$ to $\mathrm{SIRM}_{1.0\mathrm{T}}$, is used to indicate the relative contributions of ferromagnetic minerals (e.g., magnetite and/or maghemite) and antiferromagnetic minerals (e.g., hematite and/or goethite) in bulk samples (King & Channell, 1991). Hysteresis loops, IRM acquisition curves, first-order reversal curves (FORC), and -T curves were also constructed for several representatve samples. Diffuse reflectance spectroscopy (DRS) was measured for all samples using a Cary 5000 ultraviolet-visible-infrared spectrometer equipped with $BaSO_4$ as the white standard, which provided a measure of the relative hematite and goethite abundance (Zhang et al., 2018). Details for the above measurement procedures can be found in Text S3 in the supporting information.

3. Results and Discussion

3.1. Provenance discrimination

The relative abundance of clay minerals in marine sediment records can provide information on the erosional sources in the hinterland and, to some extent, on climate variability (Steinke et al., 2008). Interpreting such records require a detailed knowledge of the potential source areas, but also of the mode and strength of transport processes (Liu et al., 2010; Wan et al., 2010a). Since aeolian fluxes in the southern SCS are low (Liu et al., 2004a), terrigenous sediments in this region are mainly delivered by the surrounding rivers, such as the Mekong River and rivers from Borneo, Sumatra, the Malay Peninsula, and Thailand (Huang et al., 2016; Liu et al., 2016) (Figure 1 and 2; see also Text S1). Most of the Sunda Shelf sediments were originally supplied by the Mekong River and North Borneo rivers, with these supply routes confirmed by the presence of glacial-aged incised valleys across the Sunda Shelf (Schimanski & Stattegger, 2005) and offshore of the modern Mekong River (Tjallingii et al., 2010).

In order to interpret sediment provenance in core B9, its clay mineral assemblages (Figure S4) are compared to these potential riverine sources in a ternary diagram (Figure 2). In the absence of distinct overlap between these data and the Mekong River, northern Borneo, or other potential sources, it appears that

a mixture of sources influenced the slope area of the Sunda Shelf. Specifically, the samples of core B9 are located close to those from core CG2 (Huang et al., 2016), and most likely record a mixture of sediment sources from the Mekong River, North Borneo, and the Sunda Shelf (Figure 2). Interestingly, the clay mineral assemblages in core B9 are more closely related to the Mekong River source than the clay data from core ODP 1143 (Wan et al., 2017) (Figure 2). Such differences from core ODP 1143 presumably reflect the slightly different locations and bathymetry (Figure 1b), which enable a more direct supply from the Mekong River to cores B9 and CG2, and from the Sunda Shelf to the more southerly core ODP 1143. Overall, we consider the Mekong River and northern Borneo to be the main contributors of illite and chlorite to this region (Huang et al., 2021).

In addition, the magnetic fraction could provide complementary evidence for paleo-environmental reconstructions, based on present-day regional differences in the composition of the river-borne magnetic properties (Huang et al., 2021) (Table S2). It appears that low- to medium-coercivity (i.e. magnetically soft) minerals such as magnetite (Luzon, Taiwan, and Pearl River) and minor pyrrhotite contributions (Taiwan) dominate in the northern SCS, while high-coercivity minerals such as hematite are ubiquitous in the Mekong River, Malay Peninsula, and northern Borneo and can therefore make a significant contribution to sedimentary deposits in the southern SCS (Figure 1a) (e.g. Kissel et al., 2016, 2017). Comparing the magnetic data from core B9 (Figure S5) to the magnetic fractions of river sources, it is clear that the magnetic parameters during both glacial and interglacial times show a clear signature consistent with Mekong River sources (Table S2). Given the significantly weaker magnetization of hematite than magnetite, the low S-ratios and high HIRM values indicate the presence of abundant hematite in core B9 (Figure S5f, g).

Moreover, Torrent and Barrón (2003) suggest that the wavelength band for hematite ranges between ~535 nm and ~570 nm, according to the specific surface area of single hematite grains. Due to the Al substitution influence in the hematite crystal lattice (Liu et al., 2011), the hematite wavelength band position has previously been employed to distinguish the sources of hematite for the surface aeolian samples (Liu et al., 2015). In our study, the wavelength band fluctuates narrowly around 545 nm (Figure S5j), which suggests a fairly constant provenance for the hematite inputs. Consistent magnetic properties across glacial-interglacial cycles (Figure S6) also point to a relatively stable sediment provenance. Consequently, differences between glacial and interglacial magnetic sediment composition in the SCS (Figure 3, Figure S5) likely result mostly from changes in the sediment transport pathway and efficiency rather than from changes in the source area (Kissel et al., 2020).

3.2. Spatial and temporal heterogeneity of depositional processes

Our high-resolution record from core B9 on the southern margin of the SCS resolves climate signals over both orbital and sub-orbital timescales (Figure 3 and Figure S4-5). The smectite/(illite + chlorite) ratio (Figure 3h) exhibits similar patterns to variations in the northern SCS (Zhao et al., 2018) (Figure 3e), which were controlled by the intensity of the East Asian summer monsoon (EASM) (Cheng et al., 2016) (Figure 3b). In the northen SCS, rapid increases in the smectite/(illite + chlorite) ratio (Figure 3e) suggest a fast response to strengthened EASM rainfall (Figure 3b), which varied coincident with both precessional-scale orbital forcing (Figure 3c) and millennial-scale Dansgaard-Oeschger (DO) and Bølling-Allerød (BA) interstadial climate variability (NGRIP members, 2004) (Figure 3a). Millennial-scale oscillations in clay mineralogy driven by the EASM intensity are also present in our southern SCS record, but cannot be so clearly resolved because of its lower sedimentation rate (Figure 3h), while this variability is superimposed on a clear precessional variability. In general, a 23-kyr periodicity in the smectite/(illite + chlorite) ratio (Figure 3h) in phase with precession-driven insolation indicates that the response of clay mineralogy in the low-latitude SCS to the prevailing EASM arises rapidly, presumably mainly through changing chemical weathering intensity (Li et al., 2018b; Zhao et al., 2018).

Based on the spatial and temporal distribution of magnetic mineralogy and grain size (Figure S8), the magnetic composition of the sediments in the northern SCS remained rather uniform over the last climatic cycle. Sediment is largely supplied to the northern SCS from Taiwan and the Pearl River, with high and stable magnetite contents relative to hematite (Kissel et al., 2016, 2017). However, rock magnetic data (low S-ratio and high ratio of IRM_{AF80mT}/SIRM) from the northern SCS indicate the variable presence of some high-coercivity minerals, such as hematite coeval with maghemite (Figure 3f and 3g), which were attributed to vigorous chemical weathering (Yang et al., 2016). The deposition of these higher coercivity minerals coincided with oxygen isotope values for stalagmites (Cheng et al., 2016) (Figure 3b) and sea surface temperature (SST) reconstructions (Wei et al., 2007) (Figure 3d) that indicate a warm climate and strong EASM during the 40-90 kyr interval, suggesting a possible climate control on these inputs.

Whereas the grain size of magnetite in the northern cores was rather uniform over the last climatic cycle, it persistently fluctuated in the southern cores and was systematically coarser during glacial periods (and finer during interglacial periods) (Figure 3, Figure S8). In the northern cores, a coarser magnetic grain size was observed at the beginning of MIS 3 between 60 and 40 kyr (Figure S8d-f), but that pattern may have resulted from diagenetic processes at the inception of MIS 3 (Kissel et al., 2020). Furthermore, the controls on magnetic grain size in the northern cores are not fully understood, given a range of possible controlling factors, including ocean circulation, sea-level changes, and the

East Asian Monsoon (Chen et al., 2017). However, by analogy with the clay mineral provenance in the northern SCS, if magnetite in the northern SCS region originates mostly from Luzon and Taiwan (Liu et al., 2016; Kissel et al., 2017), then sea-level rise cannot account for the observed temporal changes due to the absence of a large continental shelf offshore of these two islands. As such, the magnetic records from the northern SCS can reflect a climatic control on the inputs, similar to the clay mineral records.

Interestingly, the hematite-rich intervals in core B9 (Figure 3i) are characterised by a coarse magnetic grain size in the southern SCS (Figure 3l), and are coincident with low hematite contents in the northern SCS (Figure 3f, g). Furthermore, the hematite content in core B9 shows a clear 23 kyr periodicity (Figure 3i), but opposite in phase to the variations in the smectite/(illite + chlorite) ratio in core B9 (Figure 3h). In the northern SCS, the lack of a major control by transport or depositional processes mean that enhanced hematite content (inferred from magnetic records) may be interpreted as a direct signature of high weathering intensity (Yang et al., 2016). In contrast, the inverse behaviour of the hematite/(goethite+hematite) fluctuations in the southern SCS indicates a different control, which we suggest arises from a combined effect of global sea-level change (Figure 3m) and ocean circulation changes. The magnetic compositions of modern river sediments indicate that hematite is abundant in rivers feeding the southern SCS, including the Red River, and the Mekong River basin (Figure 1a) (Kissel et al., 2016; 2017). Based on a comparison between the magnetic properties of core B9 and those in the potential source regions (Table S2), a large decrease in the S-ratio during glacial periods (Figure 3j) and the presence of high-coercivity minerals (Figure S5) further supports that the increased hematite contents may have been originally derived from Mekong River inputs.

There is also a close coincidence between magnetic grain-size variations (Figure 3l) and bulk sediment grain-size parameters (Figure 3k, Figure S7) in core B9, which is particularly evident in coarsening during the Last Glacial Maximum (LGM). The slightly coarser nature of the magnetic and bulk particles during glacial times could be attributed to the expansion of river channels across the shelves, which could re-suspend and transport sediments that were previously deposited on the shelves during interglacial periods and carry them to the continental slope and basin (Chen et al., 2017; Hu et al., 2012). This hypothesis of a a transport-driven control on the mineralogical records is further explored in the next section.

3.3. Differential hydrodynamic influences on terrigenous sediments in the southern SCS

Differential transport and depositional dynamics among grain-size classes may provide explanations for discrepancies in timing between weathering proxies measured at continental margin sites (Magill et al., 2018). Such hydrodynamic effects, as well as degradation during transport, could represent an intrinsic function that accounts for proxy paradoxes (Epping et al., 2002; McCave &

Hall, 2006; Mulder et al., 2013). In addition, sorting processes can also lead to differential impacts within a grain-size fraction, due to differences in properties such as particle sphericity, particle aggregation, matrix association, or mineralogy (Blattmann et al., 2019; McCave & Hall, 2006; Tesi et al., 2016).

Following previous observations that magnetic grain size varies similarly to the bulk sedimentary grain size in the North Atlantic Ocean (Kissel et al., 2013) and in the SCS (Chen et al., 2017), we consider that sea-level change and global and regional climate have led to varying hydrodynamic influences on terrigenous sediment inputs and transport in the SCS (Colin et al., 2010; Huang et al., 2019; Jiwarungrueangkul et al., 2019). We deomonstrated above that the Mekong River is the dominant source of sediments and supplies the majority of Fe oxides to core B9. The Mekong Basin has very high annual precipitation (~3000 mm/year) and temperatures (~27 °C), thereby allowing weathering rates to reach up to 150 kg/ha/year (Oliva et al., 2003). The ratio of Fe oxides is positively associated with runoff ratio, which indicates a high chemical weathering state in the Mekong Basin, but also a high discharge ability of the Mekong River (Poulton & Raiswell, 2002). Here we suggest that the inverse relationship between clay mineral and magnetic mineral tracers of chemical weathering intensity in the southern SCS in response to the EASM (Figure 3) provides support for a hypothesis of hydrodynamic influence. The siliciclasic grain-size measurements (Figure S7) indicate a robust correlation between the variation of the fine grain-size end-member EM2 (4 m) (Figure 3k) and the magnetic grain size (Figure 3l), with coarser grain sizes occuring during intervals of lower sea level (Figure 3m) and hence closer proximity to the Mekong River mouth (Figure 1).

During interglacial periods, when sea level was higher, the strong EASM led to heavy rainfall and high river runoff (Figure 4a). Under these conditions, strong erosion and weathering in the hinterland would have provided an abundant supply of smectite and hematite to the Sunda Shelf (Wan et al., 2017; Zhang et al., 2007). Previous studies have indicated that suspended load and bedload transport can lead to differential transport between the finer and coarser fractions, as recorded by changes in the radiocarbon content of sedimentary organic matter (Bao et al., 2019). Despite the longer transport distance from the Sunda Shelf to the deeper regions of the SCS at these times, fine-grained smectites could be transported in nepheloid layers (Gao & Collins, 2014; Zhu et al., 2006). As such, the clay mineral record is able to express climate-driven changes in weathering inputs linked to the EASM, although potentially further influenced by surface and intermediate water dynamics.

In contrast, the density of heavy minerals (magnetite or hematite) is too high to be significantly influenced by long-distance transport in ocean currents or nepheloid layers. Considering hematite, it is usually represented by two phases in rocks, sediments, and soils. One phase is specularite, with opaque, relatively large, and commonly euhedral crystals, whereas the other is a fine-grained, often poorly crystalline phase that provides most of the characteristic colour

of hematite. The wavelength band of hematite in B9 is at around shifts 545 nm (derived from the second derivative of the DRS spectrum), which indicates the dominance of intermediate- to coarse-grained hematite (Figure S5j). Since coarser-grained sediments are less liable to rapid seaward transport under such hydrodynamic conditions (Gao & Collins, 2014; Zhu & Chang, 2000), hematite within the coarser grain-size fractions would mostly be deposited proximally on the continental shelf (Figure 4a). Similarly, sluggish across-shelf bedload transport was observed to be accompanied by the selective degradation of organic carbon in coarser grain size fractions and a pronounced ^{14}C aging of the residual organic matter (Bao & Blattmann, 2020). As such, despite rapid formation of hematite and/or its enhanced export by rivers under conditions of a strong EASM, the amount of hematite reaching the deep sea would have been limited at these times.

The operation of such transport processes in shallow shelf regions could change with glacial-interglacial changes in sea level (Zhang et al., 2021), leading to enhanced hematite export associated with coarser-grained sediments during glacial periods (Figure 4b). Specifically, with a fall in sea level, the position of core B9 would have been closer to the paleo-Mekong River mouth, enabling the transport of silt-sized sediments to the site, primarily from the exposed Sunda Shelf (Figure 1c). The silt-sized sediments could also reflect reworking, during periods of low sea level, of the coarse detrital material that was previously deposited on the Sunda Shelf. As such, enhanced deposition of hematite during glacial periods could reflect weathering conditions from the previous (or earlier) interglacial periods rather than only the contemporaneous weathering regime, and hence it does not provide a robust indicator of weathering intensity or fluxes coincident with its deposition. Overall, this observation provides an important demonstration that hydrodynamic processes play an important role in shaping the spatial and temporal distribution of mineralogical and geochemical indicators of chemical weathering in the hinterland, and must be considered before interpreting such changes directly in terms of carbon cycle changes.

4. Conclusions

Contrasting depositional patterns among proxies hosted by different grain-size classes in sediments of the southern South China Sea over the last 90 kyr indicate the effect of differential transport dynamics by suspension and bedload transport. Fluctuations in smectite/(illite + chlorite) ratios correlate with the East Asian Summer Monsoon intensity, indicating intensification of erosion and chemical weathering in the tropical hinterland during interglacial and interstadial periods. In contrast, hematite content in the coarser fractions was subject to the influence of global sea-level change and hydrodynamic sorting, which restricted its delivery to deep sea settings until sea level fell during glacial periods. These results indicate that sea-level dynamics may be responsible for creating lead-lag patterns (or antiphasing) between proxies with similar climatic or

provenance controls but which are contained in differing grain-size classes. As such, these differential hydrodynamic influences are important factors to consider in interpretations of diverse multi-proxy down-core records, in particular when considering millennial and orbital-scale weathering and paleoclimate signals contained in terrigenous continental margin sequences.

Open Research

See https://doi.org/10.5281/zenodo.5064390 for the data acquired during this study. Table S1 and S2 are included in the supporting information.

Acknowledgements

We would like to thank the crew of the R/V Haiyang IV of Guangzhou Marine Geological Survey from the 2015 cruise. We thank Gang Li and Zhong Chen, South China Sea Institute of Oceanology, Chinese Academy of Sciences for helpful sampling and Tingwei Zhang, Sun Yat-Sen University for assistance with magnetic measurements and for providing VSM access. We also thank Monika Korte, Liao Chang, and one anonymous reviewer for their insightful input which helped us to improve the final manuscript. This work was supported financially by the National Program on National Natural Science Foundation of China (grant 41806063, 41874078, 41976065), the Laboratory for Marine Geology, Qingdao National Laboratory for Marine Science and Technology (No. MGQNLM201818), the Open Fund of the Key Laboratory of Marine Geology and Environment, Chinese Academy of Sciences (No. MGE2018KG05), the Shenzhen Science and Technology Program (Grant No. KQTD20170810111725321), and the China Postdoctoral Science Foundation (2020M682770). DJW is supported by a NERC independent research fellowship (NE/T011440/1).

References

Bao, R., & Blattmann, T. M. (2020). Radiocarbonscapes of Sedimentary Organic Carbon in the East Asian Seas. *Frontiers in Marine Science*, *7*, 517.

Bao, R., Blattmann, T. M., McIntyre, C., Zhao, M., & Eglinton, T. I. (2019). Relationships between grain size and organic carbon ^{14}C heterogeneity in continental margin sediments. *Earth and Planetary Science Letters*, *505*, 76-85.

Bao, R., Uchida, M., Zhao, M., Haghipour, N., Montlucon, D., McNichol, A., et al. (2018). Organic Carbon Aging During Across-Shelf Transport. *Geophysical Research Letters*, *45*, 8425-8434.

Berger, A. L. (1978). Long-Term Variations of Caloric Insolation Resulting from the Earth's Orbital Elements. *Quaternary Research*, *9*(2), 139-167.

Blattmann, T. M., Liu, Z., Zhang, Y., Zhao, Y., Haghipour, N., Montlucon,

D. B., et al. (2019). Mineralogical control on the fate of continentally derived organic matter in the ocean. *Science*, *366*, 742-745.

Chen, Q., Kissel, C., & Liu, Z. (2017). Late Quaternary climatic forcing on the terrigenous supply in the northern South China Sea: Input from magnetic studies. *Earth and Planetary Science Letters*, *471*, 160-171.

Cheng, H., Edwards, R. L., Sinha, A., Spötl, C., Yi, L., Chen, S., et al. (2016). The Asian monsoon over the past 640,000 years and ice age terminations. *Nature*, *534*, 640-646.

Clift, P. D., Brune, S., & Quinteros, J. (2015). Climate changes control offshore crustal structure at South China Sea continental margin. *Earth and Planetary Science Letters*, *420*, 66-72.

Colin, C., Siani, G., Sicre, M. A., & Liu, Z. (2010). Impact of the East Asian monsoon rainfall changes on the erosion of the Mekong River basin over the past 25,000yr. *Marine Geology*, *271*, 84-92.

Epping, E., van der Zee, C., Soetaert, K., & Helder, W. (2002). On the oxidation and burial of organic carbon in sediments of the Iberian margin and Nazare Canyon (NE Atlantic). *Progress in Oceanography*, *52*, 399-431.

Gao, S., & Collins, M. B. (2014). Holocene sedimentary systems on continental shelves. *Marine Geology*, *352*, 268-294.

Griffiths, M. L., Drysdale, R. N., Gagan, M. K., Zhao, J. X., Ayliffe, L. K., Hellstrom, J.C., et al. (2009). Increasing Australian–Indonesian monsoon rainfall linked to early Holocene sea-level rise. *Nature Geoscience*, *2*, 636-639.

Hanebuth, T. J. J., Stattegger, K. (2000). Rapid flooding of the Sunda Shelf: A late-glacial sea-level record. *Science*, *288*(5468), 1033-1035.

Hanebuth, T. J. J., & Stattegger, K. (2004). Depositional sequences on a late Pleistocene–Holocene tropical siliciclastic shelf (Sunda Shelf, southeast Asia). *Journal of Asian Earth Sciences*, *23*, 113-126.

Hanebuth, T. J. J., Stattegger, K., & Saito, Y. (2002). The stratigraphic architecture of the central Sunda Shelf (SE Asia) recorded by shallow-seismic surveying. *Geo-Marine Letters*, *22*, 86-94.

Hu, D., Boning, P., K € ohler, C.M., Hillier, S., Pressling, N., Wan, S., Brumsack, H.J., & Clift, P.D. (2012). Deep sea records of the continental weathering and erosion response to East Asian monsoon intensification since 14 ka in the Southe China. *Chemical Geology*, *326327*, 118.

Huang, J., Wan, S., Li, A., & Li, T. (2019). Two-phase structure of tropical hydroclimate during Heinrich Stadial 1 and its global implications. *Quaternary Science Reviews*, *222*, 105900.

Huang, J., Jiang, F. Q., Wan, S. M., Zhang, J., Li, A. C., & Li, T. G. (2016). Terrigenous supplies variability over the past 22,000 yr in the southern South

China Sea slope: Relation to sea level and monsoon rainfall changes. *Journal of Asian Earth Sciences*, *117*, 317-327.

Huang, J., Jiao, W. J., Liu, J. X., Wan, S. M., Xiong, Z. F., Zhang, J., Yang, Z. B., et al. (2021). Sediment distribution and dispersal in the southern South China Sea: Evidence from clay minerals and magnetic properties. *Marine Geology*, *439*, 106560.

Jiwarungrueangkul, T., Liu, Z., & Zhao, Y. (2019). Terrigenous sediment input responding to sea level change and East Asian monsoon evolution since the last deglaciation in the southern South China Sea. *Global and Planetary Change*, *174*, 127-137.

King, J. W., & Channell, J. E. T. (1991). Sedimentary magnetism, environmental magnetism, and magnetostratigraphy. *Reviews of Geophysics*, *29*(S1), 358-370.

Kissel., C., Van Toer, A., Laj, C., Cortijo, E., & Michel, E. (2013) Variations in the strength of the North Atlantic bottom water during Holocene. *Earth and Planetary Science Letters*, *369*, 248-259.

Kissel, C., Liu, Z., Li, J., & Wandres, C., 2016. Magnetic minerals in three Asian rivers draining into the South China Sea: Pearl, Red, and Mekong Rivers. *Geochemistry, Geophysics, Geosystems*, *17*, 1678-1693.

Kissel, C., Liu, Z., Li, J., & Wandres, C. (2017). Magnetic signature of river sediments drained into the southern and eastern part of the South China Sea (Malay Peninsula, Sumatra, Borneo, Luzon and Taiwan). *Sedimentary Geology*, *347*, 10-20.

Kissel, C., Laj, C., Jian, Z., Wang, P., Wandres, C., Rebolledo-Vieyra, M. (2020). Past environmental and circulation changes in the South China Sea: Input from the magnetic properties of deep-sea sediments. *Quaternary Science Reviews*, *236*, 106263.

Li, G., Rashid, H., Zhong, L., Xu, X., Yan, W., & Chen, Z. (2018a). Changes in Deep Water Oxygenation of the South China Sea Since the Last Glacial Period. *Geophysical Research Letters*, *45*, 9058-9066.

Li, M., Ouyang, T., Tian, C., Zhu, Z., Peng, S., Tang, Z., et al. (2018b). Sedimentary responses to the East Asian monsoon and sea level variations recorded in the northern South China Sea over the past 36 kyr. *Journal of Asian Earth Sciences*, *171*, 213-224.

Lisiecki, L. E., & Raymo, M. E. (2005). A Pliocene-Pleistocene stack of 57 globally distributed benthic ^{18}O records. *Paleoceanography*, *20*, PA1003.

Liu, Q. S., Torrent, J., Barron, V., Duan, Z. Q., & Bloemendal, J. (2011). Quantification of hematite from the visible diffuse reflectance spectrum: effects of aluminium substitution and grain morphology. *Clay Minerals*, *46*, 137-147.

Liu, Q. S., Sun, Y. B., Qiang, X. K., Tada, R., Hu, P. X., Duan, Z. Q., Jiang, Z. X., Liu, J. X., & Su, K. (2015). Characterizing magnetic mineral assemblages of surface sediments from major Asian dust sources and implications for the Chinese loess magnetism. *Earth, Planets & Space*, *67*(1), 61.

Liu, Z., Colin, C., Trentesaux, A., Blamart, D., Bassinot, F., Siani, G., & Sicre, M. A. (2004a). Erosional history of the eastern Tibetan Plateau since 190 kyr ago: Clay mineralogical and geochemical investigations from the southwestern South China Sea. *Marine Geology*, *209*, 1-18.

Liu, Z., Colin, C., Huang, W., Le, K. P., Tong, S. Q., Chen, Z., & Trentesaux, A. (2007). Climatic and tectonic controls on weathering in south China and Indochina Peninsula: Clay mineralogical and geochemical investigations from the Pearl, Red, and Mekong drainage basins. *Geochemistry, Geophysics, Geosystems*, *8*(5), Q05005.

Liu, Z., Colin, C., Li, X., Zhao, Y., Tuo, S., Chen, Z., et al. (2010). Clay mineral distribution in surface sediments of the northeastern South China Sea and surrounding fluvial drainage basins: Source and transport. *Marine Geology*, *277*, 48-60.

Liu, Z., Wang, H., Hantoro, W. S., Sathiamurthy, E., Colin, C., Zhao, Y. L., & Li, J. R. (2012). Climatic and tectonic controls on chemical weathering in tropical Southeast Asia (Malay Peninsula, Borneo, and Sumatra). *Chemical Geology*, *291*, 1-12.

Liu, Z., Zhao, Y., Colin, C., Stattegger, K., Wiesner, M. G., Huh, C. A., et al. (2016). Source-to-Sink transport processes of fluvial sediments in the South China Sea. *Earth-Science Reviews*, *153*, 238-273.

Liu, J. P., Milliman, J. D., Gao, S., & Cheng, P. (2004b). Holocene development of the Yellow River's subaqueous delta, North Yellow Sea. *Marine Geology*, *209*(1-4), 45-67.

Magill, C. R., Ausin, B., Wenk, P., McIntyre, C., Skinner, L., Martinez-Garcia, A., et al. (2018). Transient hydrodynamic effects influence organic carbon signatures in marine sediments. *Nature Communications*, *9*, 4690.

McCave, I. N., & Hall, I. R. (2006). Size sorting in marine muds: Processes, pitfalls, and prospects for paleoflow-speed proxies. *Geochemistry, Geophysics, Geosystems*, *7*, Q10N05.

Milliman, J. D., Farnsworth, K. L., & Albertin, C. S. (1999). Flux and fate of fluvial sediments leaving large islands in the East Indies. *Journal of Sea Research*, *41*, 97-107.

Milliman, J. D., & Farnsworth, K. L. (2011). River Discharge to the Coastal Ocean: A Global Synthesis. Cambridge University Press.

Mulder, T., Hassan, R., Ducassou, E., Zaragosi, S., Gonthier, E., Hanquiez, V., et al. (2013). Contourites in the Gulf of Cadiz: a cautionary note on potentially

ambiguous indicators of bottom current velocity. *Geo-Marine Letter*s, *33*, 357-367.

North Greenland Ice Core Project members. (2004). High-resolution record of Northern Hemisphere climate extending into the last interglacial period. *Nature*, *43*, 147-151.

Ohkouchi, N., Eglinton, T. I., Keigwin, L. D., & Hayes, J. M. (2002). Spatial and temporal offsets between proxy records in a sediment drift. *Science*, *298*, 1224-1227.

Oliveira, A., Vitorino, J., Rodrigues, A., Jouanneau, J. M., Dias, J. A., & Weber, O. (2002). Nepheloid layer dynamics in the northern Portuguese shelf. *Progress in Oceanography*, *52*, 195-213.

Oliva, P., Viers, J., & Dupre, B., 2003. Chemical weathering in granitic environment. *Chemical Geology*, *202*(3-4), 225-256.

Poulton, S. W., & Raiswell, R., (2002). The low-temperature geochemical cycle of iron: From continental fluxes to marine sediment deposition. *American Journal of Science*, *302*(9), 774-805.

Qi, L., Hu, J., & Gregoire, D. C. (2000). Determination of trace elements granites by inductively coupled plasma mass spectrometry. *Talanta*, *51*(3), 507-513.

Quaresma, L. S., Vitorino, J., Oliveira, A., & da Silva, J. C. B. (2007). Evidence of sediment resuspension by nonlinear internal waves on the western Portuguese mid-shelf. *Marine Geology*, *246*, 123-143.

Rohling, E. J., Grant, K., Bolshaw, M., Roberts, A. P., Siddall, M., Hemleben, Ch., & Kucera, M. (2009). Antarctic temperature and global sea level closely coupled over the past five glacial cycles. *Nature Geoscience*, *2*(7), 500-504.

Schimanski, A., & Stattegger, K. (2005). Deglacial and Holocene evolution of the Vietnam shelf: stratigraphy, sediments and sea-level change. *Marine Geology*, *214*, 365-387.

Steinke, S., Hanebuth, T. J., Vogt, C., & Stattegger, K. (2008). Sea level induced variations in clay mineral composition in the southwestern South China Sea over the past 17,000 yr. *Marine Geology*, *250*, 199-210.

Tesi, T., Semiletov, I., Dudarev, O., Andersson, A., & Gustafsson, O. (2016). Matrix association effects on hydrodynamic sorting and degradation of terrestrial organic matter during cross-shelf transport in the Laptev and East Siberian shelf seas. *Journal of Geophysical Research-Biogeosciences*, *121*, 731-752.

Thomsen, L., & Gust, G. (2000). Sediment erosion thresholds and characteristics of resuspended aggregates on the western European continental margin. *Deep-Sea Research Part I-Oceanographic Research Papers*, *47*, 1881-1897.

Torrent, J., & Barron, V. (2003). The visible diffuse reflectance spectrum in relation to the color and crystal properties of hematite. *Clays and Clay Minerals*, *51*(3), 309-317.

Tjallingii, R., Stattegger, K., Wetzel, A., & Van Phach, P. (2010). Infilling and flooding of the Mekong River incised valley during deglacial sea-level rise. *Quaternary Science Reviews*, *29*, 1432-1444.

Wan, S., Clift, P.D., Li, A., Yu, Z., Li, T., & Hu, D. (2012). Tectonic and climatic controls on long-term silicate weathering in Asia since 5 Ma. *Geophysical Research Letters*, *39*, L15611.

Wan, S., Clift, P. D., Zhao, D., Hovius, N., Munhoven, G., France-Lanord, C., et al. (2017). Enhanced silicate weathering of tropical shelf sediments exposed during glacial lowstands: A sink for atmospheric CO_2. *Geochimica et Cosmochimica Acta*, *200*, 123-144.

Wan, S., Kurschner, W. M., Clift, P. D., Li, A., & Li, T. (2009). Extreme weathering/erosion during the Miocene Climatic Optimum: Evidence from sediment record in the South China Sea. *Geophysical Research Letters*, *36*, L19706.

Wan, S., Li, A., Clift, P. D., Wu, S., Xu, K., & Li, T. (2010a). Increased contribution of terrigenous supply from Taiwan to the northern South China Sea since 3Ma. *Marine Geology*, *278*, 115-121.

Wan, S., Tian, J., Steinke, S., Li, A., & Li, T. (2010b). Evolution and variability of the East Asian summer monsoon during the Pliocene: Evidence from clay mineral records of the South China Sea. *Palaeogeography, Palaeoclimatology, Palaeoecology*, *293*, 237-247.

Wang, Y. J., Cheng, H., Edwards, R. L., Kong, X. G., Shao, X. H., Chen, S. T., et al. (2008). Millennial- and orbital-scale changes in the East Asian monsoon over the past 224,000 years. *Nature*, *451*, 1090-1093.

Wei, G. J., Deng, W. F., Liu, Y., & Li, X. H. (2007). High-resolution sea surface temperature records derived from foraminiferal Mg/Ca ratios during the last 260 ka in the northern South China Sea. *Palaeogeography, Palaeoclimatology, Palaeoecology*, *250*(1), 126-138.

Wolff, E. W., Barbante, C., Becagli, S., Bigler, M., Boutron, C. F., Castellano, E., et al. (2010). Changes in environment over the last 800,000 years from chemical analysis of the EPICA Dome C ice core. *Quaternary Science Reviews*, *29*, 285-295.

Xu, Z., Li, T., Clift, P. D., Wan, S., Qiu, X., & Lim, D. (2018). Bathyal records of enhanced silicate erosion and weathering on the exposed Luzon shelf during glacial lowstands and their significance for atmospheric CO_2 sink. *Chemical Geology*, *476*, 302-315.

Xu, Z., Wan, S., Colin, C., Clift, P. D., Chang, F., Li, T., et al. (2021). Enhancements of Himalayan and Tibetan Erosion and the Produced Organic Carbon

Burial in Distal Tropical Marginal Seas During the Quaternary Glacial Periods: An Integration of Sedimentary Records. *Journal of Geophysical Research-earth Surface*, *126*, e2020JF005828.

Xu, Z., Wan, S., Colin, C., Li, T., Clift, P. D., Chang, F., et al. (2020). Enhanced terrigenous organic matter input and productivity on the western margin of the Western Pacific Warm Pool during the Quaternary sea-level lowstands: Forcing mechanisms and implications for the global carbon cycle. *Quaternary Science Reviews*, *232*, 106211.

Yang, X., Peng, X., Qiang, X., Niu, L., Zhou, Q., & Wang, Y. (2016). Chemical Weathering Intensity and Terrigenous Flux in South China during the Last 90,000 Years—Evidence from Magnetic Signals in Marine Sediments. *Frontiers in Earth Science*, *4*, 47.

Zhang, H., Li, D. W., Sachs, J. P., Yuan, Z., Wang, Z., Su, C., & Zhao, M. (2021). Hydrodynamic processes and source changes caused elevated ^{14}C ages of organic carbon in the East China Sea over the last 14.3 kyr. *Geochimica et Cosmochimica Acta*, *304*, 347-363.

Zhang, Q., Liu, Q. S., Li, J. H., & Sun, Y. B. (2018). An integrated study of the eolian dust in pelagic sediments from the North Pacific Ocean based on environmental magnetism, transmission electron microscopy and diffuse reflectance spectroscopy. *Journal of Geophysical Research Solid Earth*, *122*(5), 3358-3376.

Zhang, Y. G., Ji, J., Balsam, W. L., Liu, L., & Chen, J. (2007). High resolution hematite and goethite records from ODP 1143, South China Sea: Co-evolution of monsoonal precipitation and El Niño over the past 600,000 years. *Earth Planetary Science Letters*, *264*, 136-150.

Zhao, S., Liu, Z., Colin, C., Zhao, Y. L., Wang, X. X., & Jian, Z. M. (2018). Responses of the East Asian Summer Monsoon in the Low-Latitude South China Sea to High-Latitude Millennial-Scale Climatic Changes During the Last Glaciation: Evidence From a High-Resolution Clay Mineralogical Record. *Paleoceanography and Paloclimatology*, *33*(7), 745-765.

Zhu, Y., & Chang, R. (2000). Preliminary study of the dynamic origin of the distribution pattern of bottom sediments on the continental shelves of the Bohai Sea, Yellow Sea and East China Sea. *Estuarine Coastal and Shelf Science*, *51*, 663-680.

Zhu, Z. Y., Zhang, J., Wu, Y., & Lin, J. (2006). Bulk particulate organic carbon in the East China Sea: Tidal influence and bottom transport. *Progress in Oceanography*, *69*, 37-60.

Zong, Y. (2004). Mid-Holocene sea-level highstand along the Southeast Coast of China. *Quaternary International*, *117*(1), 55-67.

Figure captions:

Fig. 1

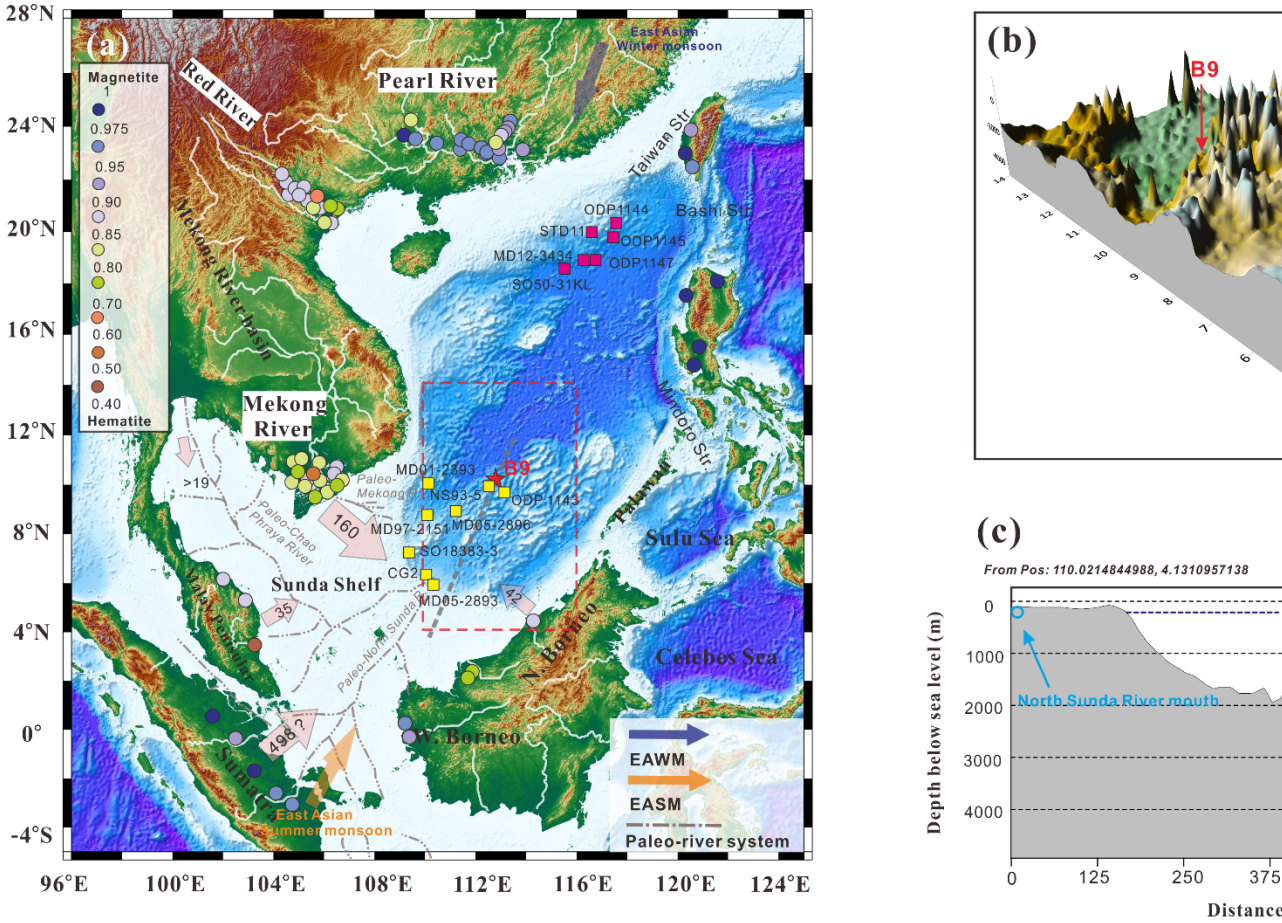

Figure 1. Geographic and bathymetric setting of the South China Sea. (a) Regional map showing the site of core B9 (red star) and, other referenced sites. Pink squares are for northern SCS sites (Kissel et al., 2020; Wei et al., 2007; Yang et al., 2016; Zhao et al., 2018), and yellow squares are for southern SCS sites (Colin et al., 2010; Huang et al., 2016; Jiwarungrueangkul et al., 2019; Kissel et al., 2020; Wei et al., 2007). The limits of the catchment basins of the Pearl, Red, and Mekong rivers are shown by white lines. Large pink arrows with numbers represent annual sediment fluxes from major local sources in Mt/yr, from Milliman & Farnsworth (2011). Distribution of the S-ratio in river sediments is illustrated with colour coded circles, indicating magnetite versus hematite content (Kissel et al., 2016; 2017). Arrows indicate modern near-surface Asian monsoon winds dominating during summer (EASM, orange) and winter (EAWM, blue). Dashed lines indicate paleo-river systmes on Sunda

Shelf. (b) Three-dimensional bathymetric map for the area marked in the red box in panel (a), showing bathymetric contours of the southern South China Sea. The topographic map was created by Surfer soft using ETOPO1 with 5 min precision. (c) Cross section, following grey dashed line in panel (a), indicating locations of the paleo-North Sunda river mouth, the studied core site B9, and the approximate Last Glacial Maximum (LGM) sea level at ~130 m below present.

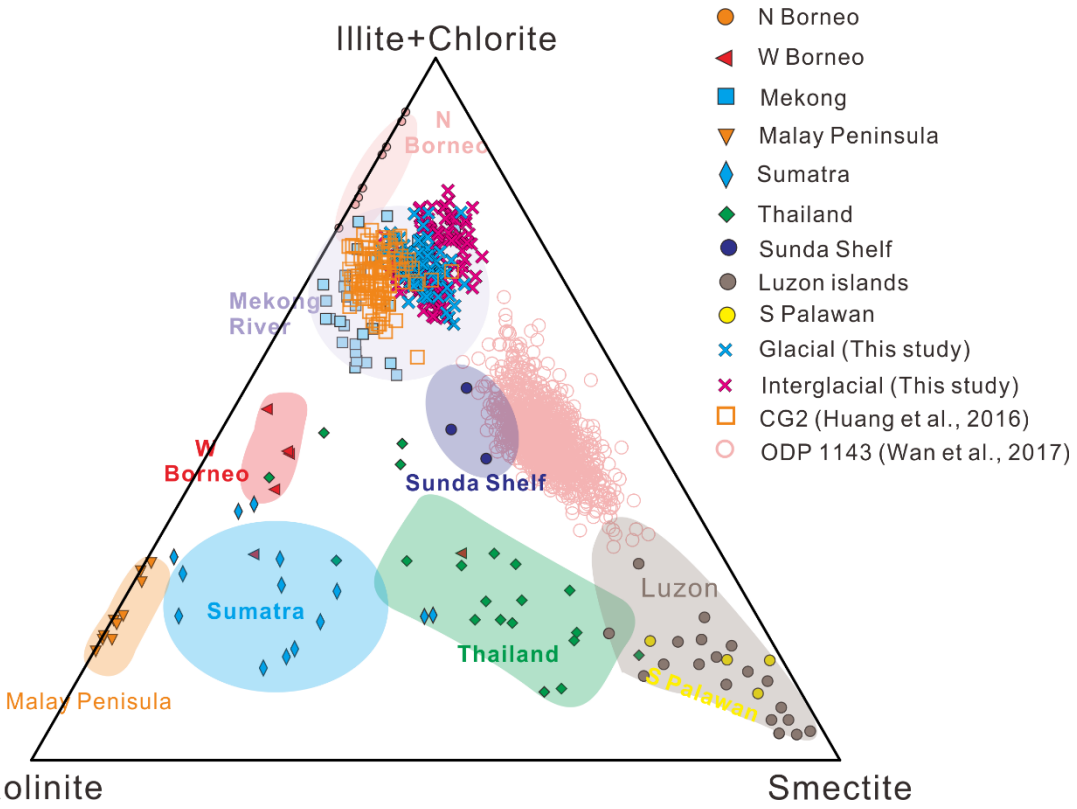

Fig. 2.

Figure 2. Ternary diagram of clay mineral assemblages in core B9 and comparison to regional sources. Glacial and interglacial data from core B9 are shown with blue and red crosses, respectively. Potential sediment sources from surrounding rivers are plotted for comparison, including the Mekong River (Wan et al., 2010b) and Thailand (Chao Phraya) river systems in the Indochina Peninsula, river systems in Sumatra and the Malay Peninsula, river systems in western (W) and northern (N) Borneo (Liu et al., 2007, 2012; Liu et al., 2016), and the Sunda Shelf (Wan et al., 2010b). Pleistocene data from cores CG2 (Huang et al., 2016) and ODP 1143 (Wan et al., 2017) are also shown.

Fig. 3.

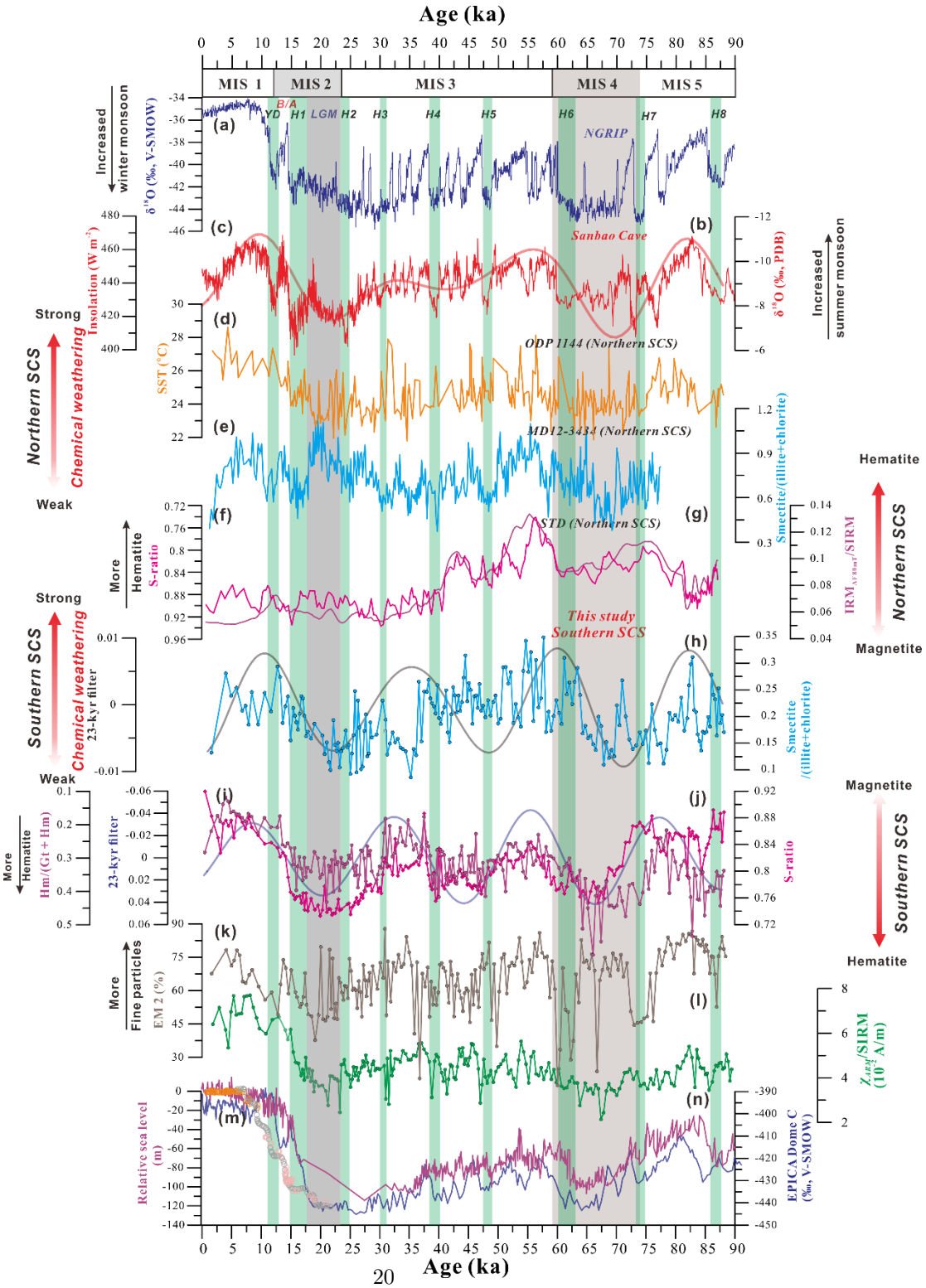
Age (ka)
MIS 1
MIS 2
MIS 3
MIS 4
MIS 5
B/A
YD
H1
LGM
H2
H3
H4
H5
H6
H7
H8
(a)
NGRIP
Increased winter monsoon
δ18O (‰, V-SMOW)
(b)
Sanbao Cave
δ18O (‰, PDB)
Increased summer monsoon
(c)
Insolation (W m-2)
Strong
Weak
Northern SCS
Chemical weathering
(d)
ODP 1144 (Northern SCS)
SST (°C)
(e)
MD12-3434 (Northern SCS)
(f)
STD (Northern SCS)
S-ratio
More Hematite
(g)
Smectite/(illite+chlorite)
IRM-0.3T/SIRM
Hematite
Magnetite
Northern SCS
This study
Southern SCS
Strong
Weak
Southern SCS
Chemical weathering
23-kyr filter
(h)
Smectite /(illite+chlorite)
(i)
Hm/(Gt+Hm)
More Hematite
23-kyr filter
(j)
S-ratio
Magnetite
Hematite
Southern SCS
(k)
EM 2 (%)
More Fine particles
(l)
χARM/SIRM (10-2 A/m)
(m)
Relative sea level (m)
(n)
EPICA Dome C (‰, V-SMOW)
Age (ka)

Figure 3. Proxy records from core B9 compared to other records over the past 90 kyr: (a) ^{18}O record from NGRIP Greenland ice core (NGRIP members, 2004); (b) stalagmite ^{18}O records from Sanbao Cave (Cheng et al., 2016); (c) 21 July insolation at 65°N (thick red curve; Berger, 1978); (d) sea surface temperature (SST) reconstruction from core ODP 1144 in the northern SCS (Wei et al., 2007); (e) smectite/(illite + chlorite) ratio in core MD12-3434 in the northern SCS (Zhao et al., 2018); (f, g) S-ratio and IRM_{AF80mT}/SIRM ratio in core STD111 in the northern SCS (Yang et al., 2016); (h) smectite/(illite + chlorite) ratio in core B9 in the southern SCS (this study), and 23 kyr Gaussian bandpass filtered output (thick purple curve); (i, j) hematite/(goethite + hematite) ratio (Hm/(Gt + Hm)) and S-ratio in core B9 in the southern SCS (this study), and 23 kyr Gaussian bandpass filtered output of Hm/(Gt + Hm) (thick blue curve); (k, l) grain-size endmember EM2 and $_{ARM}$/SIRM in core B9 (this study); (m) Relative sea level (RSL). Purple line represents global RSL (Rohling et al., 2009). Orange, grey, and pink dots represent RSL for the Southeast China Coast (Zong, 2004), East China Sea (Liu et al., 2004b), and Sunda Shelf (Hanebuth & Stattegger, 2000), respectively. (n) D record from EPICA Dome C Antarctic ice core (Wolff et al., 2010). Grey bars indicate glacial intervals and green bars indicate the Younger Dryas (YD) and Heinrich Stadials 1-8 (H1-8). B/A, Bølling-Allerød. LGM, Last Glacial Maximum. MIS, marine isotope stage.

Fig. 4.

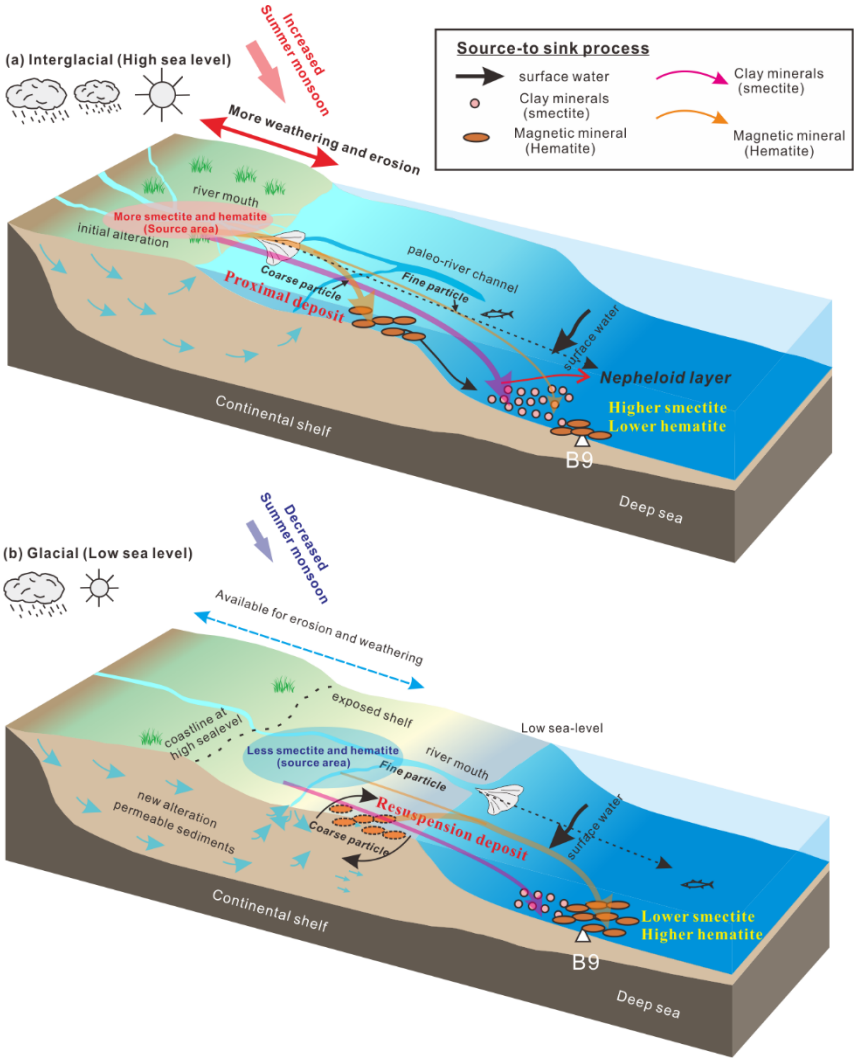

Figure 4. Conceptual model of processes that control the erosion, transport, and deposition of clays and magnetic minerals in marginal seas during (a) interglacials with high sea-level and (b) glacials with low sea-level. Figure is modified from Wan et al. (2017) based on new observations from this study.